Journal of the Mechanical Behavior of Biomedical Materials 177 (2026) 107370

Contents lists available at ScienceDirect

Journal of the Mechanical Behavior of Biomedical Materials

journal homepage: www.elsevier.com/locate/jmbbm

Comparison of the flexural strength and microstructure of 3D printed and milled mono- and multilayer zirconia

Michael Bergler [a,b,*], Andreas König [c], Jonathan Korostoff [d], Francis K. Mante [b], Sebastian Hahnel [a], Martin Rosentritt [a]

[a] University of Regensburg, School of Dentistry, Department of Prosthodontics, Regensburg, Germany
[b] University of Pennsylvania, School of Dental Medicine, Department of Restorative & Preventive Sciences, Philadelphia, PA, USA
[c] University of Leipzig, School of Dentistry, Department of Prosthodontics and Material Sciences, Leipzig, Germany
[d] University of Pennsylvania, School of Dental Medicine, Department of Periodontics, Philadelphia, PA, USA

1. Introduction

Over the past two decades, computer-aided design and computer-aided manufacturing (CAD/CAM) technology has revolutionized restorative dentistry, particularly through the adoption of high-performance ceramics. The most commonly used material for milling is yttria partially stabilized zirconia, valued for its excellent mechanical properties. Continuous improvements in material composition have led to zirconia variants with differing translucencies and flexural strengths (Dewan, 2023; Solá et al., 2021; Lestan et al., 2022; Pjetursson et al., 2018). Monolithic based zirconia restorations were introduced, using zirconia with a 3 mol% yttrium oxide (3Y-TZP: yttrium oxide-stabilized tetragonal zirconia polycrystal) content and fracture strength higher than 1200 MPa. However, due to its opacity, 3Y-TZP was primarily used for posterior restorations, as it did not meet aesthetic requirements for anterior applications. To improve translucency, manufacturers developed zirconia with 4 or 5 mol% yttrium oxide, such as 5Y-PSZ (partially stabilized zirconia; cubic zirconia) with reduced strength values of about 600 MPa. A more recent development is "Gradient Technology," which incorporates both, a color and material gradient into the milling blank. This gradient blends high-strength 3Y-TZP with a translucent 5Y-PSZ, creating a continuous transition from the cervical to incisal areas. Numerous in vivo and in vitro studies have evaluated the performance of these materials in combination with CAD/CAM technology (Pereira et al., 2023; Bernauer et al., 2025; Strasser et al., 2023; Weigl et al., 2018; Inokoshi et al., 2023; Alves et al., 2021). Despite these advances, milling remains a subtractive manufacturing process with inherent limitations. It generates material waste, increases production costs, and restricts restoration size to the dimensions of available blanks. Additionally, restoration geometry is constrained by drill diameter, axis movement, and tool angulation.

Three-dimensional (3D) printing offers an additive alternative that addresses many of these limitations. The first 3D-printed ceramic components were fabricated using stereolithography in 2000 (Doreau et al., 2000). Dentistry saw its first application in 2009, with zirconia processed via direct ink-jet printing (Ebert et al., 2009). In 2011, a complete mandible was printed in metal (Nickels, 2012), and by 2012, root analog implants were manufactured additively for immediate placement (Figliuzzi et al., 2012). Since then, interest in ceramic 3D-printing has expanded rapidly due to its precision, design freedom, and potential for cost-efficient production compared with conventional milling (Khorsandi et al., 2021; Kihara et al., 2021). Zirconia's many benefits for clinical applications in restorative dentistry have led 3D-printing companies to adopt similar material concepts for ceramic 3D-printing. Fine crown margins and accurate occlusal morphology—once difficult to achieve—are now feasible with current additive technologies (Camargo et al., 2022).

A primary limitation of dental 3D-printing has been the restricted selection of printable materials, dominated by resins. However, advances in both hardware and materials now enable fabrication of high-strength ceramics such as zirconia. Moreover, combining zirconia layers with varying yttria content allows the creation of multilayered structures that mimic the natural translucency gradient of a tooth. In milled zirconia systems, these layered compositions enhance both, esthetics and mechanical performance. With digital design and 3D-printing, these gradients can be customized more precisely to reproduce the natural tooth's internal architecture, control material distributions and potentially transforming dental manufacturing by improving efficiency and reducing material waste.

While these developments highlight the promise of additive

* Corresponding author. University of Regensburg Department of Prosthodontics, Franz-Josef-Strauß-Allee 11, 93053, Regensburg, Germany.
E-mail addresses: michael.bergler@ukr.de, mbergler@upenn.edu (M. Bergler), Andreas.Koenig@medizin.uni-leipzig.de (A. König), jkorosto@upenn.edu (J. Korostoff), mantefk@upenn.edu (F.K. Mante), Sebastian.Hahnel@klinik.uni-regensburg.de (S. Hahnel), martin.rosentritt@klinik.uni-regensburg.de (M. Rosentritt).

https://doi.org/10.1016/j.jmbbm.2026.107370
Received 14 November 2025; Received in revised form 4 February 2026; Accepted 5 February 2026
Available online 6 February 2026

manufacturing for zirconia, they also emphasize that clinical translation depends on controlling process-induced defects and the resulting mechanical strength and reliability.

At the same time, the translation of zirconia 3D printing from "printable" to clinically robust restorations are strongly constrained by process-related defect formation and the associated scatter in strength—issues that are fundamentally relevant to mechanical behavior (Harrer et al., 2017; Lu et al., 2020). Zirconia is a flaw-sensitive brittle ceramic; therefore, strength and reliability are governed by the size, type, and location of the most critical defects rather than by average density alone (Lu et al., 2020). In slurry-based lithography approaches (e.g., LCM/DLP), the manufacturing chain includes preparation and handling of a highly filled photopolymerizable zirconia suspension (Schwentenwein et al., 2015), layer-wise photopolymerization to form a "green body," and debinding and sintering to reach high density. Each of these steps can introduce characteristic flaw populations that ultimately affect characteristic strength and Weibull scatter, particularly under bending where near-surface and tensile-side defects dominate failure initiation (Harrer et al., 2017; Lu et al., 2020).

A key materials challenge is achieving stable, high solid loading with homogeneous particle dispersion while maintaining printability (rheology and recoating) (Sun et al., 2019; Jang et al., 2019; Kim et al., 2022a). Insufficient solid loading and/or dispersion can promote shrinkage gradients, trapped porosity, and agglomerates, whereas excessive viscosity can impair flowability and recoating, increasing the risk of voids and local heterogeneity (Sun et al., 2019; Jang et al., 2019; Kim et al., 2022a). In addition, zirconia's high refractive index and strong light scattering can limit cure depth and lateral fidelity, which may contribute to incomplete interlayer bonding, dimensional inaccuracies, and anisotropic shrinkage if exposure and layer parameters are not carefully optimized (Lian et al., 2018; He et al., 2018; Zhang et al., 2024; Wang et al., 2022). These phenomena are mechanically relevant because they can produce layer-interface-related defects or "weak planes" that act as preferential fracture origins (Harrer et al., 2017; Lu et al., 2020).

Thermal post-processing represents another critical bottleneck. Debinding and sintering involve large volumetric shrinkage and the development of internal stresses; inadequate thermal schedules may cause cracking, warpage, and distortion (Lian et al., 2018; He et al., 2018). Even when macroscopic defects are avoided, residual pores or elongated defects can persist and become strength-limiting flaws after sintering, as shown by fractographic and mechanical analyses of additively manufactured zirconia (Harrer et al., 2017; Lu et al., 2020). Orientation and layer architecture can further influence the effective flaw distribution because the tensile zone in flexure may intersect layer boundaries differently depending on build direction and layer thickness (Lu et al., 2020). For multilayer 3Y/5Y designs, additional complexity arises at the compositional transition: differences in powder formulation, polymerization behavior, and sintering kinetics between 3Y- and 5Y-rich regions may promote local heterogeneity and defect clustering near the interface (Zhang et al., 2024; Wang et al., 2022).

Finally, zirconia composition itself modulates sensitivity to printing-related flaws. Increasing yttria content (e.g., 5Y) improves translucency but shifts the microstructure toward higher cubic fractions and reduced transformation toughening, which can lower fracture resistance and increase sensitivity to defects and microstructural inhomogeneity (Monção et al., 2023). Consequently, it is not sufficient to generalize performance from printed 3Y-TZP to more translucent 5Y and graded 3Y/5Y systems; these materials may respond differently to identical printing and sintering conditions due to differences in phase assemblage and grain-growth behavior (Monção et al., 2023).

Despite these promising developments, limited information exists on the mechanical performance of multilayered 3D-printed zirconia compared with conventionally milled zirconia. Therefore, this study aimed to evaluate and compare the flexural strength and microstructure of 3D-printed 3Y, 5Y, and multilayered 3Y/5Y yttria partially stabilized zirconia with those of milled isostatically pressed zirconia of equivalent composition.

The null hypothesis was that 3D-printed and milled zirconia specimens with identical yttria contents 3Y, 5Y and 3/5Y would exhibit no significant differences in flexural strength and microstructural characteristics and phase composition.

2. Experimental approach

2.1. Production process

Fig. 1 shows an overview of the experimental study design.

2.1.1. Digital design

Using CAD design software (Fusion, Autodesk, San Francisco, CA, USA), bars with a geometry of 25 x 5 × 2 mm^3 were created. To minimize stress concentrations an edge chamfer of 0.12 mm (ISO 14704) was applied to the design for both milled and printed specimens for the flexural strength test. To avoid inaccuracies in the design file of the bars, the STEP file format was chosen (Zhou, 2005).

2.1.2. Printing

A total of ninety-four rectangular bars of 3D-printed 3Y, 5Y and 3/5Y multilayered yttria partially stabilized zirconia (LithaCon ceramic, Lithoz, Austria) with dimensions of 25 x 5 × 2 mm^3, were utilized for this project. The 3D-printing system CeraFab Multi 2M30 (Lithoz, Vienna, Austria) was used as the production unit.

For the single-layered 3D-printed 3Y and 5Y zirconia bars, a ceramic-loaded slurry was automatically dosed and loaded onto a transparent vat. The single-layer CAD file was used for the printing process. Layer images were generated using a digital micromirror device (DMD) coupled with a projection system, creating a three-dimensional green ceramic structure layer by layer. The lateral x, y resolution was 35 μm and the z-layer resolution was 25 μm.

For the multilayered 3Y/5Y zirconia bars, two vats were used: one was loaded with 3Y material, and the second one was loaded with 5Y material. The multilayered CAD file was used for this process: the design was divided into two identical layers: an upper layer (50% for 5Y) and a lower layer (50% for 3Y). First, the lower part of the sample was printed with 3Y and after completing this cycle, the sample was automatically transferred to the vat containing the 5Y material. All specimens were printed horizontally, so that the samples assigned to the component platform came to rest in the bending zone of the bending beams.

After the printing process was finished, a thermal post-processing step was conducted to remove the binder, and the green appliance was sintered, resulting in a fully dense ceramic part. According to manufacturer's instructions, the sintering temperature was at 1450 °C with a 2-h dwell time (Fig. 2). For the sintering a high temperature furnace (Thermoconcept HTL 10/17, Bremen, Germany) was used. Sintering was performed with sintering beads according to the manufacturer's recommendations with the flat surface down. The time for thermal post-processing was 74 h total.

3D-printed bars after final sintering of the multilayered material 3Y/5Y and the single layered printed 3Y material are shown in Fig. 3 (3Y position was marked with a dot).

2.1.3. Milling

A total of 94 bars of monolayer 3Y, 5Y and multilayered 3/5Y yttria partially stabilized, isostatic-pressed zirconia (Prettau®, Prettau 4 Anterior® and Prettau 3 Dispersive® Zirconia, Zirkonzahn, Italy) with the same dimensions were fabricated using a five-axis simultaneous milling machine (M4, Zirkonzahn, Gais, Italy). Milling was performed dry. The single-layered CAD file was used for the production process. Three different bur sizes 2.0 mm, 1.0 mm and 0.5 mm were used for milling to achieve a detailed and smooth surface finish of the samples.

After milling, the 3Y (Prettau®) pre-sintered zirconia was sintered

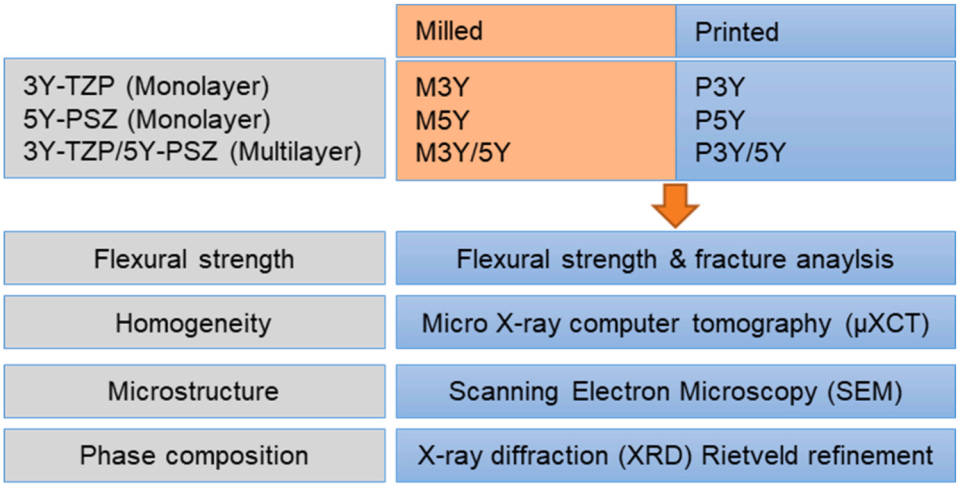

Fig. 1. Overview experimental design.

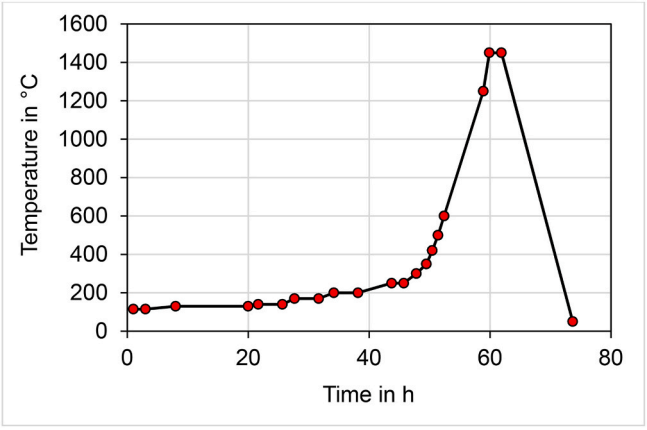

Fig. 2. De-binding and sinter schedule for 3D printed zirconia samples (Provided by Lithoz).

according to manufacturer's instructions at 1600 °C with a 2-h dwell time to produce fully dense ceramic parts. Sintering was performed with sintering beads according to the manufacturer's recommendations with the flat surface down. The 5Y material (Prettau 4 Anterior®) and the 3Y/5Y multilayered (Prettau 3 Dispersive®) were sintered at 1500 °C with a 2-h dwell time, following the manufacturer's guidelines. The sintering furnace (Zirkonofen 600/V3, Zirkonzahn, Gais, Italy) was used to sinter the milled samples.

All the samples have been fabricated within the same 3D orientation, horizontal to the z-axis. For the milled samples a blank with 12 mm in heights was chosen and the samples have been placed at 6 mm to meet the layer transition of 3Y to 5Y of the graded material. This resampled the same yttria distribution of the milled multilayered samples compared to the printed samples with a predefined 50% 3Y and 50% 5Y layer distribution.

After fabrication all specimens were wet-polished with silicone carbide paper (Tegramin-25, Struers, D; grit of 4000; wet; P1200) to final dimensions 25 x 5 × 2 mm^3 +/−0.08 mm.

2.2. Investigations

2.2.1. Flexural strength

For the flexural strength test, the milled and 3D-printed zirconia bars were divided into six groups (Table 1), (n = 30 per material and group). The dimension of the bars was 25 x 5 × 2 mm^3 +/− 0.08 mm and the testing span length was set to 20 mm.

Flexural strength was determined using a three-point bend test on a universal testing machine (Instron 4204, Norwood, MA, USA) with a 5000 N load cell following ISO 6872:2024. The force F during the flexural strength test was applied perpendicular to the Z-axis of the specimens at a loading rate of 1 mm/min. The multilayer specimens were positioned so that the 3Y side was always the tensile stress side (bottom) and the 5Y side was always the compressive stress side (top).

2.2.2. Homogeneity (micro X-ray computer tomography (µXCT))

In order to detect inhomogeneity in the microstructure, micro-X-ray computed tomography (µXCT) measurements were carried out on two samples of each material (n = 2 per group). An industrial tomograph with a microfocus X-ray tube (FXE 225.99, YXLON International GmbH, Hamburg, Germany)) and flat detector (1621xN 2D detector, PerkinElmer (Waltham, MA, USA) was used. The following settings were used for the measurements: focal spot 0.6 µm, beam energy 180 kV/180 µA

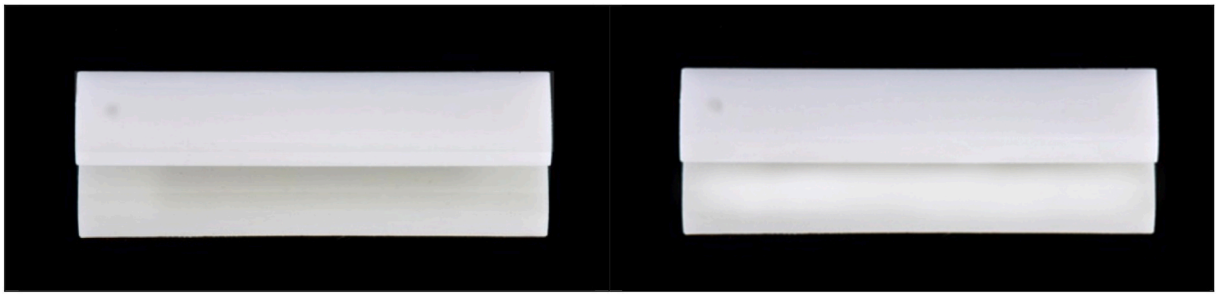

Fig. 3. Left multilayered printed zirconia sample with a layer distribution of 50% 3Y on the bottom and 50% 5Y on the top. Right: Single layered 3Y printed zirconia sample.

Table 1
Overview of the ZrO_2 materials used with the manufacturing processes and information (n.i.: no information available).

Name	Manufacturing process	Y_2O_3 mol%	Company, Material	Composition	Properties
M3Y	Milling	Monolayer 3 mol%	Zirkonzahn, Prettau®	Y_2O_3: 4 – 6 %; Al_2O_3: max. 1 %; SiO_2: max. 0,02 %; Fe_2O_3: max. 0,01 %, Na_2O: max. 0,04 %;	Flexural strength 1000 – 1200 MPa; Hardness (HV10) 1250 HV10; Weibull-Modulus ~ 15
M5Y	Milling	Monolayer 5 mol%	Zirkonzahn, Prettau Anterior®	Y_2O_3: max 12 %; Al_2O_3: max. 1 %; SiO_2: max. 0,02 %; Fe_2O_3: max. 0,01 %	Flexural strength 670 MPa; Hardness (HV10) 1250 HV10; Weibull-Modulus ~ 15
M3/5Y	Milling	Multilayer 3/5 mol%	Zirkonzahn, Prettau 3 Dispersive®	Mixture of M3Y and M5Y	n.i.
P3Y	Printing	Monolayer 3 mol%	Lithoz, LithaCon ceramic 3Y	Y_2O_3: 3 %	Flexural strength 770 MPa; Hardness (HV10) 1250 HV10; Weibull-Modulus <25
P5Y	Printing	Monolayer 5 mol%	Lithoz. LithaCon 5Y	Y_2O_3: 4 – 6 %	n.i.
P3/5Y	Printing	Multilayer 3/5 mol%	Lithoz, LIthaCon 3Y/5Y	Mixture of P3Y and P5Y	n.i.

and, step size of 0.225° (1600 steps/360°). A voxel edge length of 7 μm was achieved with this setup. The inhomogeneities were visualized with the software "ImageJ 1.47 v" (National Institutes of Health, Bethesda, MD, USA) and "VGStudioMax" (version 2.0, Volume Graphics GmbH, Heidelberg, Germany) and quantified in its geometry.

2.2.3. Microstructure (Scanning Electron Microscopy (SEM))

SEM imaging (Quanta FEG 400, FEI, USA) was used to visualize the individual microstructure of each material and layer. Specimens from the fracture test were examined at magnifications between 1,00 and 30,000x (Low vacuum; WD: 9.4 – 10.7 mm; HV: 15 keV).

2.2.4. Phase composition (X-ray diffraction (XRD) incl. Rietveld refinement)

The phase composition of the monolithic samples of each material was analysed by powder X-ray diffraction (XRD) using MINIFLEX 600 (Rigaku, Tokyo, Japan). The multilayer samples were examined on both the top and bottom sides, and the monolayer samples were examined on one side (n = 2 per group). The Samples were arranged in the correct orientation and irradiated with Cu Kα radiation (1.5418 Å, 40 kV 10 mA) and measured between 10 and 140° diffraction angle. A DTex Ultra 2 MF (Rigaku, Tokyo, Japan) was used as the detector. The search match routine and Rietveld refinements were performed with SMARTLAB Studio II v5.0.174.0 (Rigaku, Tokyo, Japan). Apart from the errors in the weight percentages of the phase fractions, the errors of the software were adopted. An error of 1-2% (Jansen et al., 2011) by mass was assumed for the weight percentages, because of the higher R_{wp}-values.

2.2.5. Statistical analysis

Median flexural strength and quartiles were calculated for the six experimental groups. One Way Anova and Bonferroni test was used for individual comparison (α = 0.05) Weibull analysis was used to determine characteristic strength and Weibull modulus. Parameter estimates are based on Maximum Likelihood Estimation (MLE). The significance level (α) was set to α = 0.05.

3. Results

3.1. Flexural strength

Median flexural strength values and Weibull results for the six printed and milled zirconia groups are shown in Table 2. Median flexural strength varied between 433.7 MPa (M5Y) and 1008.5 MPa (M3Y) in the milled group and between 296.2 MPa (P5Y) and 722.9 MPa (P3Y) in the printed group. Individual comparison revealed significant differences between M3Y and P3Y (p = 0.001) but not between M5Y and P5Y (p = 0.108) or M3/5Y and P3/5Y (p = 0.068; F: 68,410, Sig: <0.001, $\eta^2 = 0.663$ and observed power = 1.000).

Mean characteristic strength varied between 433.7 MPa (M5Y) and 1034.4 MPa (M3Y) in the milled group and between 342.5 MPa (P5Y) and 824.9 MPa (P3Y) in the printed group. Weibull modulus was higher for the milled groups (5.8-7.9) in comparison to the printed groups (2.9-4.3)(Fig. 4).

3.2. Homogeneity

3.2.1. Homogeneity (micro X-ray computer tomography (μXCT))

μXCT measurements identified few defects in all printed samples (Table 3), but no defects in the milled samples. The defects in the two printed monolayers were distributed across the entire samples (Fig. 5), while the defects in the multilayer sample were concentrated in the transition area between the two layers.

3.2.2. Microstructure (Scanning Electron Microscopy (SEM))

Representative SEM micrographs collected across magnifications of 100 × , 1000 × , and 20,000 × for 3Y and 5Y (milled vs. 3D-printed), 100 × and 10,000 × for 3Y/5Y (milled and 3D-printed), and 400 × and 30,000 × for the top (5Y-rich) and bottom (3Y-rich) layers of the graded materials are shown in the assembled figure set.

At low magnification (100 ×), all groups exhibited continuous, crack-free surfaces without visible layer lines or interface defects. Compared to the milled sample, a large number of black dots can be seen

Table 2
Median flexural strength (MPa) with quartiles, characteristic flexural strength (MPa) and Weibull modulus (−) (identical letters indicate significant differences, p < 0.05) Parameter estimates based on maximum likelihood estimation (MLE, Coefficient of determination ($r^2 > 0.95$).

Group	Flexural Strength Median	25%	75%	Characteristic flexural strength	Weibull modulus	5%	95%	Sum Likelihood	Mean life (μ)	Variance (σ^2)
Group 1 (M3Y)	1008.5 ^{a,b,c,d,e}	882.9	1057.5	1034.4	7.9 ^{A,B,C,D,E}	6.9	10.7	−12,469	975	18,367
Group 2 (M5Y)	433.7 ^{a,f,g,h}	368.7	481.7	433.7	5.8 ^{A,F,G,H,I}	4.6	7.1	−18,657	428	7030
Group 3 (M3/5Y)	869.8 ^{b,f,i}	705.7	968.3	869.8	6.9 ^{B,F,J,K,L}	5.5	8.5	−16,465	844	19,012
Group 4 (P3Y)	740.8 ^{c,g,j}	548.5	882.3	824.9	3.2 ^{C,G,J,M}	2.8	4.4	−11,813	736	47,117
Group 5 (P5Y)	296.2 ^{d,i,j,k}	239.4	379.1	342.5	4.3 ^{D,H,K,M,N}	3.6	5.6	−13,265	311	7224
Group 6 (P3/5Y)	722.9 ^{e,h,k}	502.8	954.2	810.0	2.9 ^{E,I,L,N}	2.5	3.9	−12,307	722	59,746

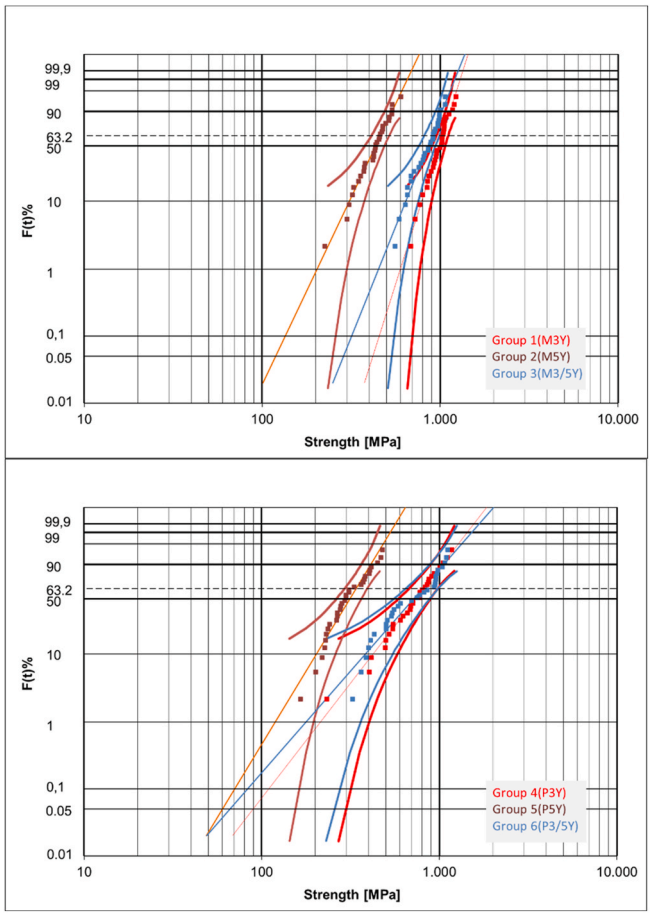

Fig. 4. Weibull Plot of the results (above milled, below 3D printed materials).

on the printed P3Y sample (red arrows). These dots increase in concentration and intensity towards the edges of both samples (red circles) In the 5Y materials, the picture here seems much more balanced: Small black areas accumulate on the upper side of the P5Y samples, while these tend to be larger on the M5Y and are distributed throughout the material.

At 1000 × , the printed surfaces appeared microscopically more inhomogeneous than the milled surfaces. Here, it can be seen that the size of the black dots (red arrows) in the printed P3Y material, at approximately 25 µm, seams significantly larger than those in the milled system (max. 1 µm). In this magnification, there is hardly any difference between the materials M5Y and P5Y. At high magnification (mainly 20,000 × ; 30,000 × for the layer-resolved views), dense, fine microstructures were visible in each group, but the 3D-printed samples exhibited more breakouts/microvoids and occasionally more inhomogeneous-looking areas than their milled counterparts in both 3Y and 5Y. This enlargement clearly shows that the milled material has larger grains than the printed material. However, both materials exhibit non-homogeneous grain sizes across the entire image section, indicated by blue (small grains) and red (big grains) arrows. The effect is even more pronounced for the M5Y and P5Y materials. However, here too, there is a clear difference in grain size between printed and milled materials. (Fig. 6).

In the graded 3Y/5Y systems (Fig. 7), no strong differences were found between the layers. However, for the P3Y/5Y, separation lines appeared to run between the layers (red arrow). With greater magnification, the transitions and grain boundaries for the printed material are more clearly visible (arrows with different colours). With higher magnifications (10 000x) the top (5Y-rich) regions appeared more heterogeneous with bigger grains, while the bottom (3Y-rich) regions were finer and more uniform. The printed material has clearly different grain sizes, while the milled material appears more variable in grain size, but is rather homogeneous over the entire transition. No discrete delamination or sharp interfaces were observed—rather, the microstructural appearance transitioned smoothly with increasing depth.

Details of the edges of the samples (Fig. 8), indicate that printed groups and 5Y-rich regions appeared more defect-bearing/coarser than milled groups and 3Y-rich regions. This seems consistent with the trends inferred from porosity and mechanical data. While the printed material shows a clear difference in grain size (bottom-top), the grains of the milled material appear to be of similar size.

3.2.3. Phase composition (X-ray diffraction (XRD) incl. Rietveld refinement)

Y-richer thermodynamically more stable tetragonal T' and Y-poorer regular T phases were detected in most of the samples. The t' phase with larger lattice parameters occurred particularly in areas with no or little (only 3Y printed) cubic phase content. The cubic phase (C) was identified predominantly (with the exception of 3Y printed) in all 5Y printed/milled samples and on the 5Y side of the multilayer samples. The thermodynamically most stable monoclinic phase was detected exclusively in milled/printed 3Y as well as 3Y/5Y samples on the 3Y side. The rhombohedral phase (R) was identified exclusively in all milled 5Y samples (both mono- and multilayer) (Figs. 9 and 10).

4. Discussion

The null hypothesis that 3D-printed and milled zirconia specimens with identical yttria contents 3Y, 5Y and 3/5Y would exhibit no significant differences in flexural strength, microstructure and phase composition could be partly confirmed.

4.1. Flexural strength

No significant statistically differences were found between the milled vs. 3D-printed 5Y or milled vs. 3D-printed multilayered 3Y/5Y zirconia. Overall, the 3D-printed groups in tendency exhibit lower mean flexural strength than milled zirconia. The Weibull modulus and characteristic strength are lower for printed materials and also show greater quartile differences. A lower Weibull modulus indicates higher variability in failure stress for the printed groups. Most samples show the failure crack typical of the classic 3-point bending test in the tensile zone, with a characteristic compression zone in the compressive zone. Given the material and testing properties, it can be assumed that the fracture begins in the tensile zone; however, the critical defect could be located on the surface, below the surface, or in the bulk. The homogeneity analysis

Table 3
Number of defects, equivalent defect diameter based on their volume and defect content in relation to one bending beam.

Defects	Units	M3Y	P3Y	M5Y	P5Y	M3Y/5Y	P3Y/5Y
Number of defects[a]	-	0	1	0	30	0	3
diameter of the largest defect [b]	µm	-	158	-	238	-	52
Content	‰	-	0.0086	-	0.0117	-	0.0009

[a] only closed defect in the structure, not on the surface.
[b] defects equivalent defect diameter based on their volume.

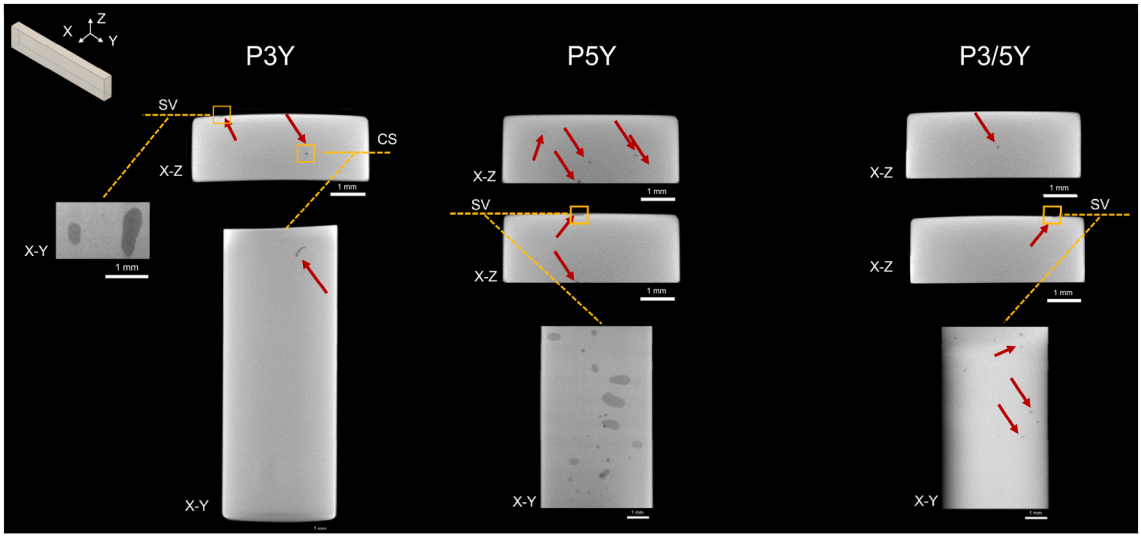

Fig. 5. Sectional views (SV) of the three printed materials; the red arrows point to defects in the samples. (For interpretation of the references to colour in this figure legend, the reader is referred to the Web version of this article.)

from µXCT confirms the higher number of defects for print material, especially P3Y/5Y. However, the defects in the multilayer material are the smallest and the lowest in percentage terms. In contrast, the larger grain structure of the milled samples actually indicates low strength. The cause of the low strength of the printed samples might therefore be found in the homogeneity and structure of the printed sample. SEM images also show an indication of an accumulation of black dots at the edges of the samples, which might contribute to the fracture performance of the specimens. A comprehensive, thorough, and detailed fractographic examination should therefore be carried out on all samples in the future.

Evidence on 3D-printed zirconia beyond 3Y remains limited: most recent studies address 3Y, while only a few evaluate 5Y, and none so far address multilayer systems (Alghauli et al., 2024). Reported flexural strength for 3D-printed 3Y commonly exceeds 800 MPa, meeting ISO 6872:2024 class 5 indications (Kim et al., 2022b; Zandinejad et al., 2022; Revilla-León et al., 2021a; Zenthöfer et al., 2022; Pinelli et al., 2025). Our printed 3Y mean was lower than those reports. Differences across studies likely reflect material formulation, specimen preparation, printing/sintering parameters, and test setup (Mohammed et al., 2024). Notably, our samples size n = 30 per group follows ISO recommendations for Weibull analysis and provides higher power than many prior studies (n = 5-15). For 5Y, two studies reported values < 150 MPa--comparable to leucite-based glass-ceramic-potentially due to thinner bars (≈1.2 mm), differing solid loadings, printing processes, porosity, or test conditions (Teegen et al., 2023; Revilla-León et al., 2021b; Attar et al., 2023). In our data, printed 5Y fell within the lithium disilicate range and did not differ from milled 5Y zirconia.

For printed multilayer 3/5Y, no prior data exist. We used a 50% 3Y and 50% 5Y distribution and 0° print orientation to mimic clinical layering. From a processing perspective, 3D-printing builds parts layer-by-layer, inter-layer bonding is typically weaker than intra-layer bonding, making inter-layer strength a critical determent of the mechanical performance (An et al., 2019).

4.2. Homogeneity

The absence of defects in milled samples is attributable to the industrial manufacturing process of the blanks, in which the powder is uniaxially pressed and isostatically recompacted. The number of defects with a min. size of approximal 14 µm (double resolution for µXCT measurements) in the printed samples was very low (max. 0.0086 ‰). For this reason, it is not surprising that the flexural strengths of milled samples were only slightly higher than those of printed samples. Pores and agglomerates are more likely to appear at the joint of the layers, which – as a result – is commonly the weak area of the final products (Harrer et al., 2017). Not surprisingly, µXCT identified most defects in the printed multilayer sample in the center of the specimen. Therefore, it is necessary to optimize the printing parameters to make the interlink areas more inseparable. At present, the application technologies of 3D-printing in dentistry are mainly based on slurry, and the conventional wisdom is that an appropriate ratio of powder and liquid is essential for 3D-printing. A high ratio of powder to liquid relates to smaller pores and agglomerates in the product. Nevertheless, if the ratio is too high, flowability is impaired, making it easier to settle. It is reported, solid loads below 50% result in ZrO_2 parts with low density, significant shrinkage, and defective pieces (Lian et al., 2018) (Sun et al., 2019; He et al., 2018). The slurry ratio for the production of our samples is unknown, since not all details are shared by companies for confidentiality reasons. However, the zirconia slurry used for printing dental products usually has a high viscosity. Air bubbles may consequently get entrapped during the printing process. If these air inclusions are located in the highly tensile stressed region of the specimens, they can spread across multiple layers and create worm-like pores, which eventually become fracture origins (Mei et al., 2021). They can be distributed throughout various parts of the product, especially on the surface (Lu et al., 2020). According to research, the porosities are classified into cavities for shrinkage and gas holes. Through experimental verification and theoretical analysis, it was shown that the air conveyed by powder spraying injection into the molten pool was the primary cause of the creation of pores (Yan et al., 2019). However, differences were identified in the fracture initiations of DLP (Digital Light Processing) specimens, which were mainly reflected in the proportion, location, and size of fracture initiating pores (Lu et al., 2020). More printing parameters and sintering programs related to porosity and agglomerates should become future research topics. It is significant to find a balance between a large enough solid load and good flowability. The consistency of the slurry produced for printing determines the mechanical properties of the final products. Slurry using large particles and high dry matter content can ensure good and reliable density, flexural strength and Weibull modulus. On top of that, as zirconia has a high refractive index and scatters light strongly, photopolymerization typically results in significant incident light scattering. As a result, the photopolymer's cure depth is constrained, and anisotropic contraction takes place (Jang et al., 2019). According to a study, the solid loading needs to be at least 40% in order to prevent flaws following debinding and sintering (Sun et al.,

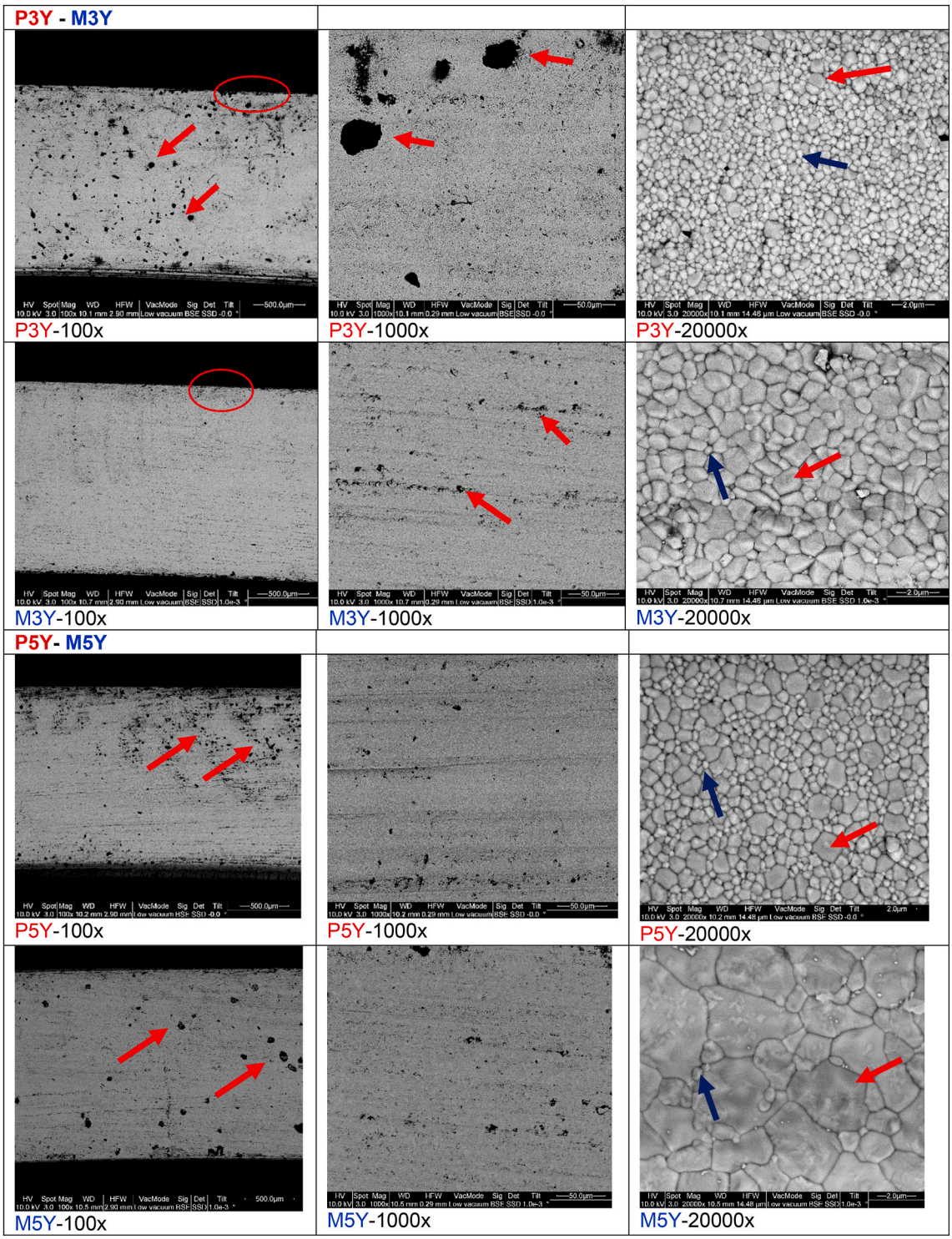

Fig. 6. SEM of 3Y and 5Y 3D Printed & Milled samples at 100x, 1000x, 20000x.

2019).The viscosity will significantly increase when the solid content exceeds 60% (Kim et al., 2022a). Researchers conducted experiments using a slurry containing 58% zirconia and obtained satisfactory mechanical properties (Lu et al., 2020; Mei et al., 2021).

4.3. Microstructure

SEM analyses did not support the study hypothesis that milled, and 3D printed zirconia specimens do not show differences in SEM microstructure. Nevertheless, the grain size appears to be larger in ground materials than in 3D-printed materials. The reason for this remains unclear, but could be due to the raw material and the manufacturing process. The grain size and structure of the grains certainly affects aging, such as LTD of the zirconia materials. Phase transformations are likely to occur more frequently and on a significantly larger scale in smaller grains and 3Y (Spies et al., 2020) For 3Y, a dramatic increase in the proportion of monoclinic phase is to be expected, whereas for 5Y a more moderate increase of up to 10% should be sufficient. However, aging is not solely attributable to grain size. The picture becomes clearer when examining the phase fraction. 3Y fractions show no cubic areas and, in

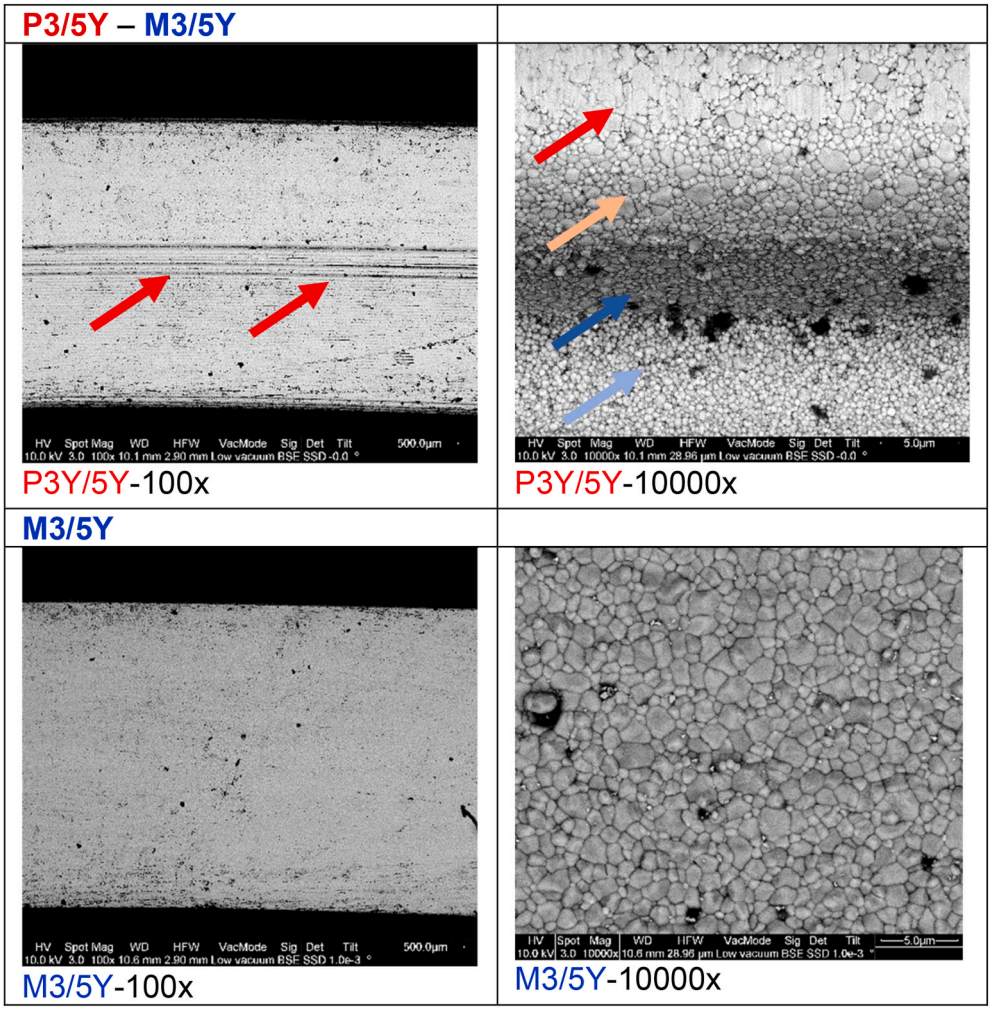

Fig. 7. SEM 3Y/5Y 3D printed & milled at 100x & 10000x.

addition, even rhombohedral fractions. Earlier studies have shown an increased monoclinic phase content for 3Y, whereas no transformability of 5Y-PSZ was found: Reduced strength of 5Y samples as compared to 3Y may be associated with deficient transformability in the fracture (Spies et al., 2020). Monoclinic zirconia was observed at the fractured surfaces of 3Y, indicating stress-induced transformability, whereas no stress-induced transformability was detected at the fractured surfaces of 5Y samples. At low magnification (100 ×), all groups appear macroscopically continuous and crack-free, with no visible build-layer signatures - suggesting that any print-induced banding is below the contrast/resolution of SEM imaging at this scale. The assessment is supported by CT results, which showed only few isolated defects in the entire beam.

By 1000 × magnification, printed surfaces look microscopically rougher than milled ones, and at higher magnifications (10,000 × ; 30,000 × for layer views) printed fields more often exhibit pull-outs/micro-voids and coarser-appearing patches than their milled counterparts. Compositionally, the 5Y materials (and the 5Y-rich "top" zones of the graded samples) appeared coarser and more heterogeneous, whereas 3Y and the 3Y-rich "bottom" zones displayed finer and more uniform areas. In the graded 3Y/5Y systems, the change in appearance was gradual with depth and no discrete interfacial defects were evident - an encouraging sign for layer integrity. Within a given layer, field-to-field variability is limited; heterogeneities concentrated in 5Y-rich regions.

The SEM analyses consistently corroborate a microstructural tendency towards more defect-bearing/coarser-appearing regions in 3D-printed and 5Y-rich conditions versus milled and 3Y-rich ones. This visual narrative aligns with known material behavior (greater cubic fraction in 5Y, reduced transformation toughening) and offers a mechanistic context for differences observed with other modalities in this study. The phenomenon can be attributed to the slurry content and lower sintering temperatures (1450 °C) of the 3D printed samples compared to the milled counterparts, which are sintered at temperatures between 1550 °C and 1600 °C. With an increase in slurry solid content and sintering temperature, the microstructure becomes denser, and grain sizes increase. A sintering temperature of 1400 °C produces microstructures with a significant number of micropores, which indicates that they cannot be fully sintered at this temperature (Zhang et al., 2024; Wang et al., 2022).

4.4. Phase composition

In accordance with the phase diagram of Y_2O_3 - ZrO_2 system, the XRD results demonstrated that the cubic phase fraction increases with rising Y fraction (Lipkin et al., 2013). Our SEM images show, supported by previously published data, that the cubic phase is accompanied by larger grain sizes, which leads to a significant decrease in fracture toughness and, thus, strength (Strasser et al., 2023; Monção et al., 2023). The relationship between grain size and fracture toughness as well as strength is based on the so-called Hall-Petch effect (Wang et al., 2025; Willems et al., 2019).

The monoclinic (M) phase fraction indicates a phase transformation

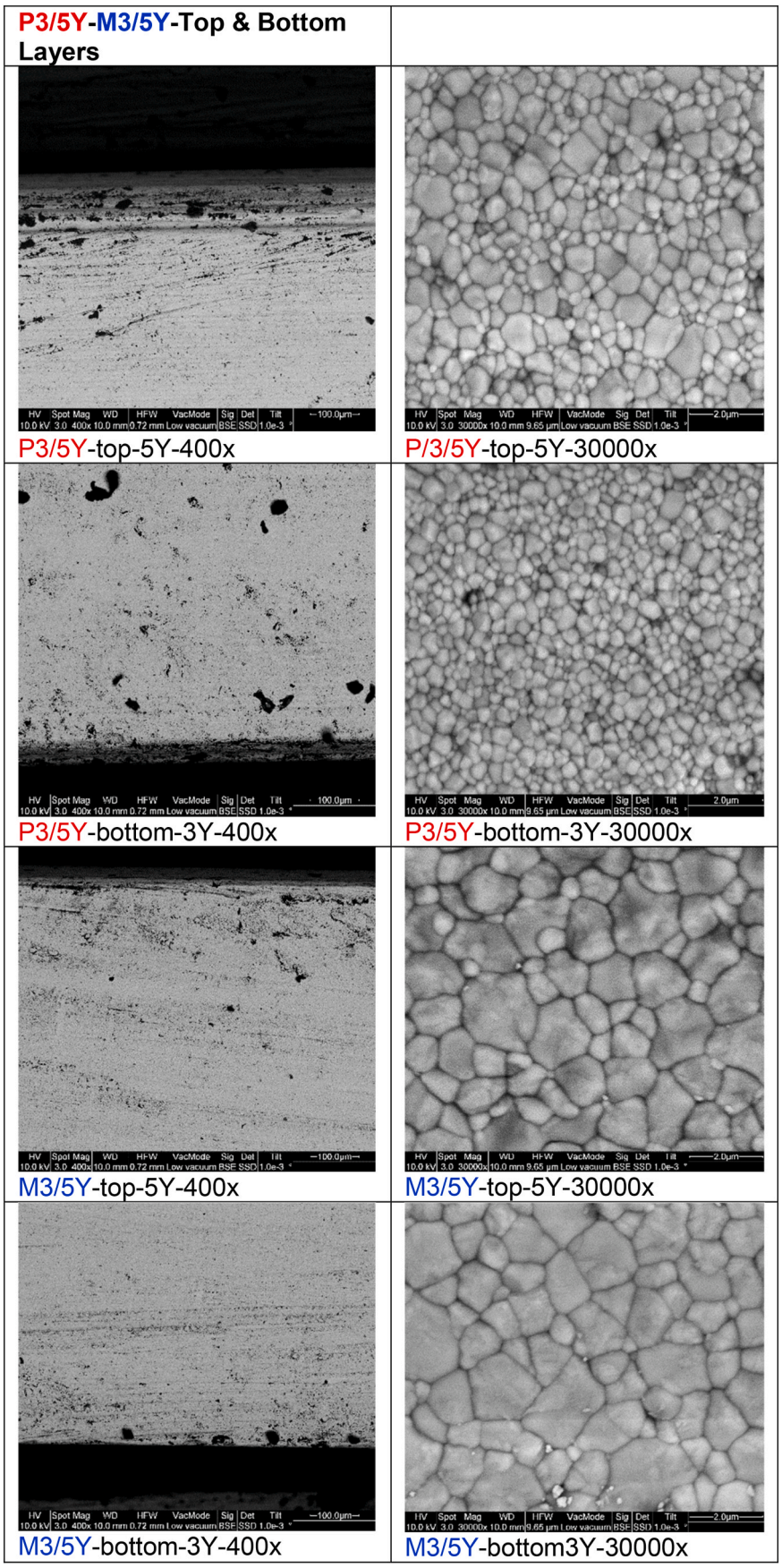

Fig. 8. SEM detailed layers of 3Y/5Y layers of 3D printed and milled samples at 400x and 30000x.

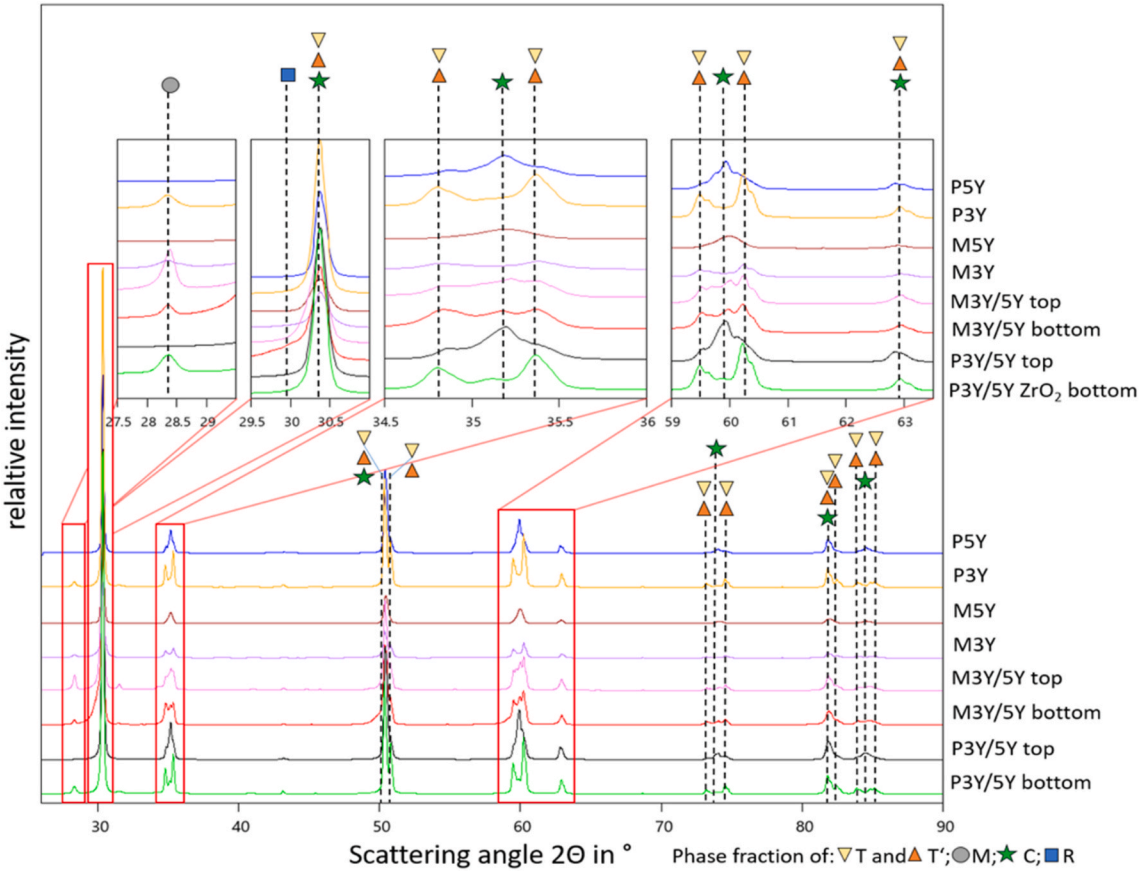

Fig. 9. Diffractograms in overview (below) and in detail (above) depending on the sample surfaces.

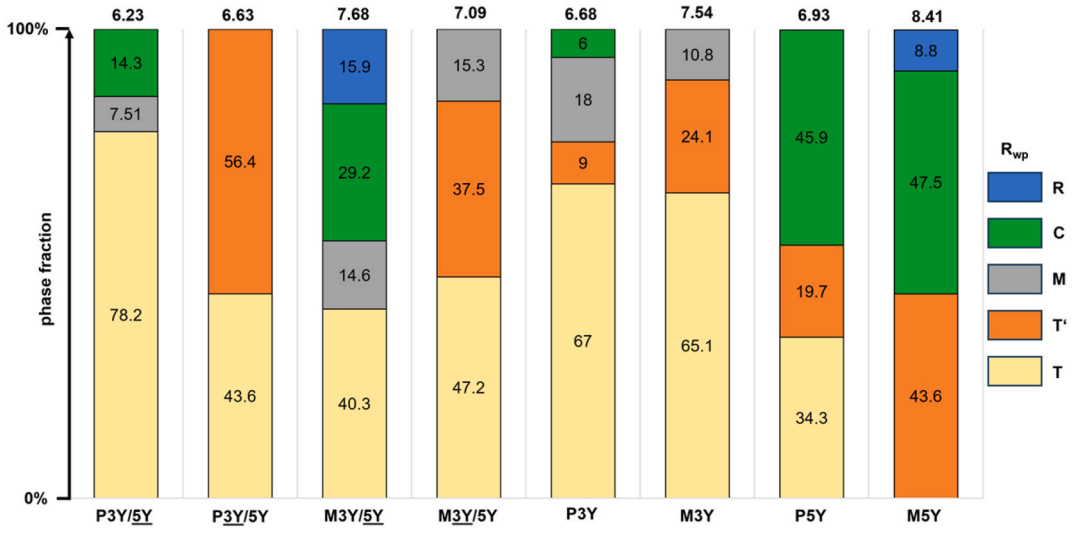

Fig. 10. Phase fraction (weight percentages; Rietveld refinement of the measured PXRDs).

from the tetragonal (T) phase, especially for 3Y with the lowest Y partial stabilisation, which is well known in the literature (Wertz et al., 2021). In contrast, no monoclinic phase could be detected in 5Y mono- or multilayer samples, as the cubic phase is thermodynamically more stable due to the larger grain size and higher Y content (as is the T' phase). The phase transformation occurs independently of the layer type (mono vs. multi) and the manufacturing process (printing vs. milling) in all samples with 3Y. In 5Y samples, however, the metastable rhombohedral phase (R) was detected on the surface, which is described in the literature as occurring under low mechanical/thermal influences such as grinding or polishing (Wertz et al., 2024).

4.5. Clinical relevance and limitations

Multilayer 3D-printed zirconia offers the potential to simply produce specimens with built-in shade/translucency gradients and patient-specific geometries while simplifying workflows and reducing material waste. The data of the current study show similar flexural strength for

milled and printed 3Y/5Y and 5Y zirconia, which underlines its clinical feasibility. However, printed groups showed lower reliability (Weibull) and more micro-defects in SEM/μCT analyses, which may increase chipping or catastrophic failure risk—especially in areas under high mechanical stress, such as in connectors. When designing restorations in a clinical setting, peak stresses should be kept in 3Y-rich zones and minimum thickness/connector guidelines should be respected, followed by careful surface finishing (and possibly HIP/glaze) to mitigate flaws (Müller et al., 2025). Key limitations of the current study include process sensitivity (slurry viscosity/green density, debinding/sintering windows), batch variability, and limited long-term fatigue/aging evidence compared with established milled materials. The results of this laboratory studies are also limited by the choice of raw materials and the parameters and equipment used in the manufacturing process and should be verified with alternative products and boundary conditions in further studies. In addition, other properties relevant to clinical implementation, such as surface texture and the influence of ageing processes, should be investigated.

5. Conclusion

Overall, the 3D-printed groups in tendency exhibit lower mean flexural strength, Weibull modulus and characteristic strength than milled zirconia. The homogeneity analysis from μXCT confirms the higher number of defects for print material, especially P3Y/5Y.

Milled zirconia therefore continues to demonstrate superior strength, microstructural integrity, and overall reliability. Although 3D printing shows mechanical potential for highly translucent 5Y and 3Y/5Y multilayer zirconia, its clinical applicability is currently constrained by a greater susceptibility to defects and reduced reliability. Further optimization of the printing and sintering processes - particularly at interlayer transition zones seems essential to ensure safe and reliable clinical use. A comprehensive, thorough, and detailed fractographic examination should therefore be carried out on all samples in the future.

CRediT authorship contribution statement

Michael Bergler: Writing – review & editing, Writing – original draft, Visualization, Validation, Supervision, Project administration, Methodology, Investigation, Data curation, Conceptualization. **Andreas König:** Writing – review & editing, Writing – original draft, Resources, Methodology, Investigation. **Jonathan Korostoff:** Writing – review & editing. **Francis K. Mante:** Writing – review & editing, Investigation. **Sebastian Hahnel:** Writing – review & editing. **Martin Rosentritt:** Writing – review & editing, Investigation.

Declaration of competing interest

The authors declare that they have no known competing financial interests or personal relationships that could have appeared to influence the work reported in this paper.

Data availability

Data will be made available on request.

References

Alghauli, M.A., et al., 2024. The physical-mechanical properties of 3D-printed versus conventional milled zirconia for dental clinical applications: a systematic review with meta-analysis. J. Mech. Behav. Biomed. Mater. 156, 106601.

Alves, M.F., et al., 2021. Mechanical properties and translucency of a multi-layered zirconia with color gradient for dental applications. Ceram. Int. 47 (1), 301–309.

An, D., et al., 2019. A strategy for defects healing in 3D printed ceramic compact via cold isostatic pressing: sintering kinetic window and microstructure evolution. J. Am. Ceram. Soc. 102 (5), 2263–2271.

Attar, E.A., Aldharrab, A., Ajaj, R., 2023. Flexural strength properties of five different monolithic computer-aided Design/computer-aided manufacturing ceramic materials: an in vitro study. Cureus 15 (3).

Bernauer, S.A., et al., 2025. Flexural strength of translucent zirconia for single crowns and fixed dental prostheses—A systematic review. J. Prosthodontic Res. p. JPR_D_24_00277.

Camargo, B., et al., 2022. 3D printing and milling accuracy influence full-contour zirconia crown adaptation. Dent. Mater. 38 (12), 1963–1976.

Dewan, H., 2023. Clinical effectiveness of 3D-Milled and 3D-Printed zirconia Prosthesis-A systematic review and meta-analysis. Biomimetics 8 (5).

Doreau, F., Chaput, C., Chartier, T., 2000. Stereolithography for manufacturing ceramic parts. Adv. Eng. Mater. 2 (8), 493–496.

Ebert, J., et al., 2009. Direct inkjet printing of dental prostheses made of zirconia. J. Dent. Res. 88 (7), 673–676.

Figliuzzi, M., Mangano, F., Mangano, C., 2012. A novel root analogue dental implant using CT scan and CAD/CAM: selective laser melting technology. Int. J. Oral Maxillofac. Surg. 41 (7), 858–862.

Harrer, W., et al., 2017. Fractography of zirconia-specimens made using additive manufacturing (LCM) technology. J. Eur. Ceram. Soc. 37 (14), 4331–4338.

He, R., et al., 2018. Fabrication of complex-shaped zirconia ceramic parts via a DLP-stereolithography-based 3D printing method. Ceram. Int. 44 (3), 3412–3416.

Inokoshi, M., et al., 2023. Layer characteristics in strength-gradient multilayered yttria-stabilized zirconia. Dent. Mater. 39 (4), 430–441.

Jang, K.-J., et al., 2019. Effect of the volume fraction of zirconia suspensions on the microstructure and physical properties of products produced by additive manufacturing. Dent. Mater. 35 (5), e97–e106.

Jansen, D., et al., 2011. Does ordinary Portland cement contain amorphous phase? A quantitative study using an external standard method. Powder Diffr. 26 (1), 31–38.

Khorsandi, D., et al., 2021. 3D and 4D printing in dentistry and maxillofacial surgery: printing techniques, materials, and applications. Acta Biomater. 122, 26–49.

Kihara, H., et al., 2021. Applications of three-dimensional printers in prosthetic dentistry. J. Oral Sci. 63 (3), 212–216.

Kim, J., et al., 2022a. Effect of dispersants on structural integrity of 3D printed ceramics. Int. J. Appl. Ceram. Technol. 19 (2), 968–978.

Kim, M.-S., et al., 2022b. Microstructure, flexural strength, and fracture toughness comparison between CAD/CAM milled and 3D-Printed zirconia ceramics. Appl. Sci. 12 (18), 9088.

Lestan, N.G., et al., 2022. Clinical evaluation of monolithic zirconia multiunit posterior fixed dental prostheses. J. Prosthet. Dent 128 (6), 1258–1264.

Lian, Q., et al., 2018. Additive manufacturing of ZrO2 ceramic dental bridges by stereolithography. Rapid Prototyp. J. 24 (1), 114–119.

Lipkin, D.M., et al., 2013. Phase evolution upon aging of air-plasma sprayed t′-Zirconia coatings: I—synchrotron X-ray diffraction. J. Am. Ceram. Soc. 96 (1), 290–298.

Lu, Y., et al., 2020. Flexural strength and weibull analysis of Y-TZP fabricated by stereolithographic additive manufacturing and subtractive manufacturing. J. Eur. Ceram. Soc. 40 (3), 826–834.

Mei, Z., et al., 2021. Determination of hardness and fracture toughness of Y-TZP manufactured by digital light processing through the indentation technique. BioMed Res. Int. 2021 (1), 6612840.

Mohammed, M.K., et al., 2024. Evaluation of zirconia ceramics fabricated through DLP 3d printing process for dental applications. Heliyon 10 (17), e36725.

Monção, A., et al., 2023. Effect of Y 2 O 3 content on the mechanical and optical properties of zirconia-based dental ceramics. Cerâmica 69, 278–287.

Müller, M.M., et al., 2025. The effect of surface treatment and glass-ceramic coating on the wear behavior of different types of zirconia and their antagonists. Quintessence Int. 56 (6).

Nickels, L., 2012. World's first patient-specific jaw implant. Met. Powder Rep. 67 (2), 12–14.

Pereira, R.M., et al., 2023. A comparative study of mechanical properties of yttria stabilized zirconia monolithic and bilayer configuration for dental application. J. Mech. Behav. Biomed. Mater. 148, 106160.

Pinelli, L.A.P., Ferreira, I., Dos Reis, A.C., 2025. Analysis of flexural strength and weibull modulus of printed and milled zirconia: a systematic review. J. Prosthet. Dent.

Pjetursson, B.E., et al., 2018. A systematic review of the survival and complication rates of zirconia-ceramic and metal-ceramic single crowns. Clin. Oral Implants Res. 29 (Suppl. 16), 199–214.

Revilla-León, M., et al., 2021a. Flexural strength and weibull characteristics of stereolithography additive manufactured versus milled zirconia. J. Prosthet. Dent 125 (4), 685–690.

Revilla-León, M., et al., 2021b. Flexural strength and weibull characteristics of stereolithography additive manufactured versus milled zirconia. J. Prosthet. Dent 125 (4), 685–690.

Schwentenwein, M., Homa, J., 2015. Additive manufacturing of dense alumina ceramics. Int. J. Appl. Ceram. Technol. 12 (1), 1–7.

Solá-Ruiz, M.F., et al., 2021. Prospective study of monolithic zirconia crowns: clinical behavior and survival rate at a 5-year follow-up. J Prosthodont Res 65 (3), 284–290.

Spies, B.C., et al., 2020. Reliability and aging behavior of three different zirconia grades used for monolithic four-unit fixed dental prostheses. Dent. Mater. 36 (11), e329–e339.

Strasser, T., et al., 2023. Microstructure, composition, and flexural strength of different layers within zirconia materials with strength gradient. Dent. Mater. 39 (5), 463–468.

Sun, J., Binner, J., Bai, J., 2019. Effect of surface treatment on the dispersion of nano zirconia particles in non-aqueous suspensions for stereolithography. J. Eur. Ceram. Soc. 39 (4), 1660–1667.

Teegen, I.S., et al., 2023. Comparison of properties and cost efficiency of zirconia processed by DIW printing, casting and CAD/CAM-milling. Dent. Mater. 39 (7), 669–676.
Wang, B., et al., 2022. The influence of microstructure on the flexural properties of 3D printed zirconia part via digital light processing technology. Materials 15 (4), 1602.
Wang, L., et al., 2025. Effect of grain size on mechanical properties and aging of yttria-stabilized tetragonal zirconia polycrystal fabricated by stereolithography-based additive manufacturing. Ceram. Int. 51 (2), 1613–1622.
Weigl, P., et al., 2018. In-vitro performance and fracture strength of thin monolithic zirconia crowns. The journal of advanced prosthodontics 10 (2), 79–84.
Wertz, M., et al., 2021. The influence of surface preparation, chewing simulation, and thermal cycling on the phase composition of dental zirconia. Materials 14 (9), 2133.
Wertz, M., et al., 2024. Phase transformations in yttria-partly stabilized zirconia induced by dental polishing regimes. J. Mater. Sci. 59 (15), 6476–6496.
Willems, E., et al., 2019. Iron oxide colouring of highly-translucent 3Y-TZP ceramics for dental restorations. J. Eur. Ceram. Soc. 39 (2-3), 499–507.
Yan, S., et al., 2019. 3D printing of nano-scale Al2O3-ZrO2 eutectic ceramic: principle analysis and process optimization of pores. Addit. Manuf. 28, 120–126.
Zandinejad, A., et al., 2022. The flexural strength and flexural modulus of stereolithography additively manufactured zirconia with different porosities. J. Prosthodont. 31 (5), 434–440.
Zenthöfer, A., et al., 2022. Strength and reliability of zirconia fabricated by additive manufacturing technology. Dent. Mater. 38 (10), 1565–1574.
Zhang, F., et al., 2024. Fabrication of zirconia ceramic dental crowns by digital light processing: effects of the process on physical properties and microstructure. 3D Print. Addit. Manuf. 11 (3), e1257–e1270.
Zhou, M.Y., 2005. STEP-Based approach for direct slicing of CAD models for layered manufacturing. Int. J. Prod. Res. 43 (15), 3273–3285.